ACS NANO

www.acsnano.org

ARTICLE

Three-Dimensional Visualization of Oxygen-Vacancy Migration and Redistribution in Ca-Substituted $BiFeO_3$

Bingqian Song, Heung-Sik Park, Jeonghun Suh, Jeongdae Seo, Jihun Kim, and Chan-Ho Yang*

Cite This: *ACS Nano* 2024, 18, 1948–1957

Read Online

ACCESS | Metrics & More | Article Recommendations | Supporting Information

ABSTRACT: **Ionic movement has received renewed attention in recent years, particularly in the field of ferroelectric oxides, since it is intrinsically linked to chemical reaction kinetics and ferroelectric phase stability. The associated surface electrochemical processes coupled local ionic transport with an applied electric bias, exhibiting very high ionic mobility at room temperature based on a simple electrostatics scenario. However, few studies have focused on the applied-polarity dependence of ionic migration with directly visualized maps. Here, we use incorporated experiments of conductive scanning probe microscopy and time-of-flight secondary ion mass spectrometry to investigate oxygen ionic migration and cation redistribution in ionic oxides. The local concentrations of oxygen vacancies and other cation species are visualized by three-dimensional mappings, indicating that oxygen vacancies tend to be ejected toward the surface. An accumulation of oxygen vacancies and ionic redistribution strongly depend on tip polarity, thus corroborating their role in the electrochemical process. This work illustrates the interplay between ionic kinetics and electric switching.**

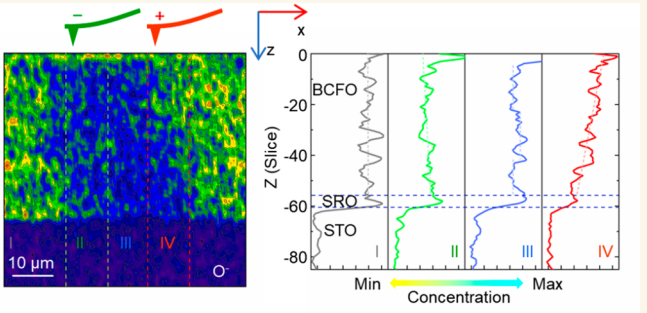

KEYWORDS: *Ca-substituted $BiFeO_3$, oxygen vacancy, ionic migration, cation redistribution, time-of-flight secondary ion mass spectrometry, conductive-AFM*

Defect engineering of vacancies, antisite defects, interstitials, and chemical substitutions by donors/acceptors each provide a promising method for controlling local electronic properties and relevant electrochemical behaviors.[1−4] The cation redistribution of electrochemical modulation couples intrinsically to their physical properties, for example, in ferroelectrics, emerging enhanced conductivity at predefined domain walls,[5] ultrafast ionic mobility,[6,7] chiral topology,[8] and more.[9−11] The associated surface reaction kinetics are switched with electric polarization; furthermore, induced metastable states are considered as the signature of logical memory devices[12] and superionic conductors.[13] Thus, for materials with high ionic mobilities, an opportunity arises to carefully study the interplay between ionic motion and electric polarity (e.g., ferroelectric switching[14,15]). This still remains poorly understood and is critical for investigating degradation and fatigue processes in ferroelectrics, for example.

Our model materials, Ca-doped bismuth ferrites with a significantly lower oxygen-migration activation energy, E_A, have been exploited for many years. By creating solid solutions between orthorhombic $CaFeO_{2.5}$ (brownmillerite)[16] and monoclinic $BiFeO_3$ (perovskite),[17] defect engineering has emerged as a versatile tool for tuning the electronic and optoelectronic properties of these materials, meeting the practical demands of application in electrochromic sensors,[6] resistive-switching memories,[18,19] solid-state fuel cells,[20−22] and batteries.[23] $BiFeO_3$-parent oxides undergo a ferroelectric-to-paraelectric transition with increasing calcium ion concentration. Naturally induced oxygen vacancies (V_O) are confined to crystallographic unit cells due to the presence of Ca^{2+} acceptors and the intrinsic maintenance of the valence state of Fe^{3+}. With regard to oxygen stoichiometry and transport, a study of bulk ceramics showed spontaneous V_O creation and mixed electronic and ionic conductions, as reported by Masó et al.[24] The ionic conductivity was characterized rapidly in epitaxial

Received: July 19, 2023
Revised: December 27, 2023
Accepted: January 2, 2024
Published: January 11, 2024

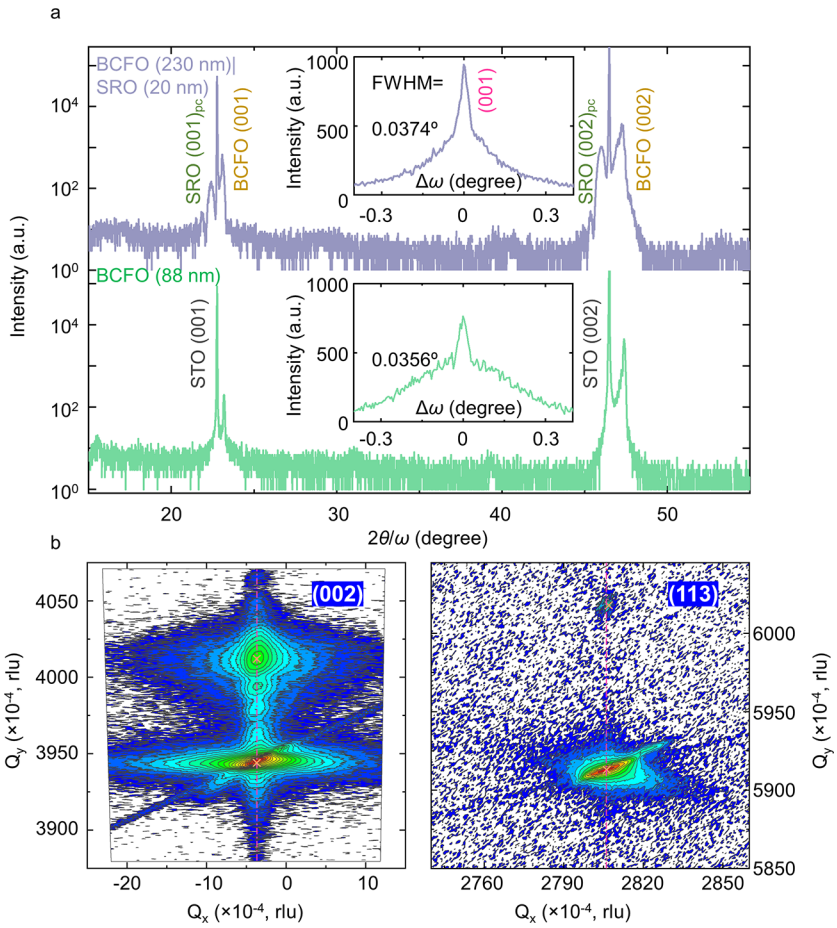

Figure 1. Structural characterization of BCFO epitaxial films. (a) XRD $2\theta-\omega$ scans for two different BCFO film thicknesses. The film thickness is determined by the Scherrer formula. The insets represent ω-scans for rocking curves at BCFO (001) reflection. (b) X-ray RSMs for symmetric (002) and asymmetric (113) reflections. All ×'s mark the (002) and (113) central reflections of the BCFO thin films and STO substrates, respectively.

films,[18] and a significantly large ionic mobility of 2×10^{-6} cm^2 s^{-1} V^{-1} was recorded at 390 °C.[20] Extensive studies show the films have self-assembled superlattice structures with periodic V_O channels that microscopically arrange in order along ⟨100⟩ or ⟨110⟩ crystal axis across the critical Ca doping ratio of x_{Ca} = 0.45.[7] The possible scenario on ionic conductivity involved positively ionized V_Os moving in external electric fields, which was preliminarily verified by an electro-coloration approach associated with the filamentary conduction pathways.[25,26] Once the mobile donors are electrically removed, the optical color of the electrically formed region transforms into a dark color from inborn yellow, being electronically hole-doped.[10] Despite these efforts, the direct probing of the ionic motion (V_Os possibly) governed by an external electrical stimulus has remained out of reach in our Ca-substituted $BiFeO_3$ system. Thus, the key questions now are whether the V_O motion appears under an external bias and how it affects the local conductivity, which is still poor in real-space experiments.

The motion of V_Os is usually coordinated by differences in the spatial distribution of the atomic-scale oxygen lattice, so the alteration of the oxygen lattice, in turn, determines the injection or rejection of oxygen at structural (sub)lattice sites. This enables direct imaging of a structural lattice in real space with a sub-nanometer or ångstrom resolution, for example, through the use of a transmission electron microscope (TEM). In one case, the field-mediated migration of V_Os was imaged with time-resolved TEM combined with an *in situ* scanning probe microscopy, where nanoscale structural stripes, which are associated with the existing V_Os, were induced by tip bias and relaxed as the external field was dismissed thereafter,[27] similar to the case of field-induced crystal dislocation motion.[28] Those sublattice visualizations with real-time experiments on defect motion, however, were not widely used for functional analysis, and this limits the processing approaches and engineering applications of most crystalline materials. In another case, advanced multimodal chemical imaging techniques simultaneously offer physical information coupled with nanoscale chemical information, such as mass spectrometry with a combination of high-resolution optical microscopy. Major advantages of time-of-flight secondary ion mass spectrometry (TOF-SIMS) include its substantial lateral resolution and sufficient mass resolution for isotope-level separation. By visualizing active ingredients inside, the tool can be used to define the spatial distribution and kinetics of various phenomena, such as tracer diffusion of isotropies,[29,30] fatigue of metals,[31] degradation of (in-)organic materials,[14] phase transitions,[32] drug delivers,[33] and so on.[15,34−37] Its strength lies in the ability to simultaneously detect and identify multiple chemical clusters within three-dimensional space while providing sufficient depth resolution to distinguish a unit cell. For example, the approach was used to explore that screening charges required for thermodynamic stability of a ferroelectric

https://doi.org/10.1021/acsnano.3c06675
ACS Nano 2024, 18, 1948−1957

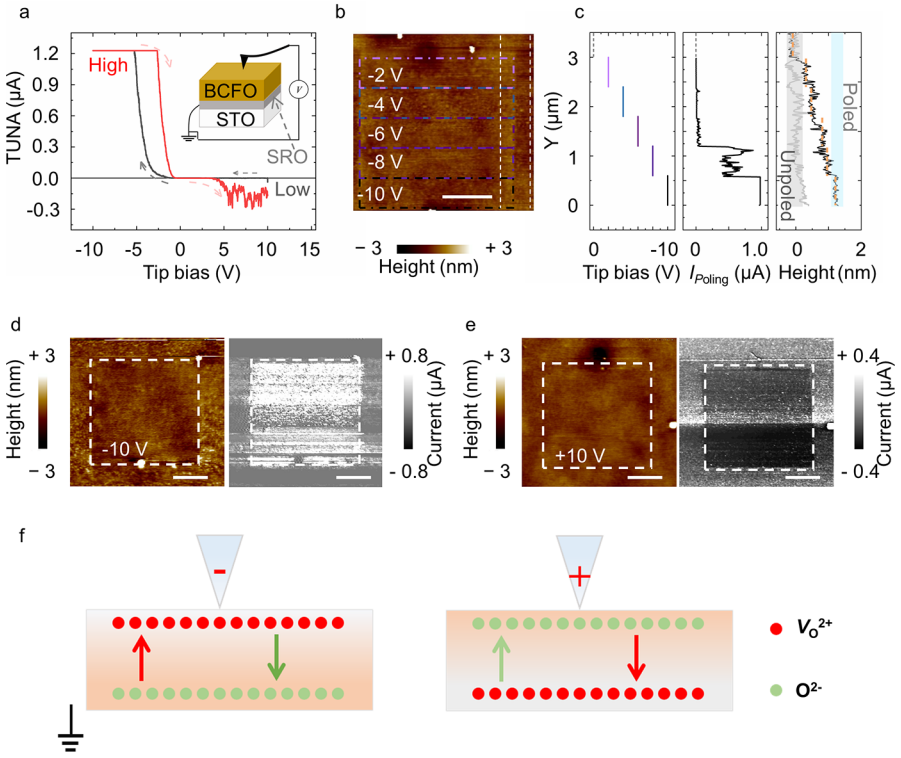

Figure 2. Electrical modulation under a biased SPM/AFM tip. (a) Resistive switching behaviors by point current−voltage (I−V) curves using the Bruker TUNA module. The arrows indicate the cycle of switching (in a sequence of +10 V → 0 V → − 10 V → 0 V → +10 V of tip bias), and the inset shows the schematic setup for cAFM experiments. The sweep from +10 to −10 V in the gray line indicates the local low-conductance state, while the red line from −10 to +10 V represents the high-conductance state. (b) Strain modulation by electrochemical reaction under electrical poling by incrementally increasing the negative tip-bias voltage, showing the different expansion of lattice structure. Different colored rectangles for each poling process are shown with the size of 3 μm × 0.6 μm. The scale bar in white represents 1 μm. (c) Line profiles of tip bias, poling currents, and topographic heights along two vertical dashed lines in b. (d, e) cAFM images of the patterned area under the poling bias of −10 V and +10 V, respectively. Topographic images after electrical poling show no significant surface damage or morphological change (left), and the current map (right) with a reading bias of −2.0 V shows an enhanced-conductivity modulation (−10 V) and a current-suppression behavior (+10 V). The scale bar represents 1 μm, and the current scale in the left and right ones represents 0.8 and 0.4 μA, respectively. (f) Schematic illustration of the possible electrochemical mechanism under different polarity biases.

domain induced ionic motion and modified compositions at surface layers (<3 nm).[38] Furthermore, due to recent advances, it is highly possible to study related crystal-defect dynamics, which are largely unknown experimentally in greater detail and with improved accuracy.[28,38] This information could further be used for carefully investigating the physical and chemical phenomena associated with local polarity reversal in ferroelectrics and other complex oxides.

In the present work, we provide a visualization strategy to study the V_Os' motion under an external applied bias. Different from ferroelectric switching of the parent oxide, the electrical modulation in Ca-doped $BiFeO_3$ is significantly involved with ionic motions. In the combined study of conductive-AFM (cAFM) and TOF-SIMS, we investigate the polarity effect of an external bias that drives the forward motion of V_Os and cation redistribution in nanoscale and then locally control its electrical conductivity and strain dependence, indicating the dominant role of V_O-assisted electrochemical reactions at the film surface. Three-dimensional visualization maps establish possible changes of the sample composition and specifically define the enrichment layer of V_Os in the vicinity of a freshly poled region. The motion of V_Os is regulated back and forth independently, depending on the direction of the electric field, and both negatively and positively poled ionic distributions are directly resolved. This work highlights the importance of the chemical interplay of ion transport and associated physical properties, especially the promising application of tip-bias-mediated electrochemistry in electrolytes.

RESULTS AND DISCUSSION

Epitaxial films of $Bi_{0.4}Ca_{0.6}FeO_{3-\delta}$ (BCFO) were grown on (001) $SrTiO_3$ (STO) substrates by pulsed laser deposition, which involved ablating a homemade BCFO target. The crystalline structure, film thickness, and strain state were analyzed by X-ray diffraction (XRD) through 2θ−ω scans and reciprocal space maps (RSMs). The anticipated diffraction peaks and thickness fringes were observed in a symmetric XRD scan along the [00L] direction, demonstrating the crystallinity of epitaxial BCFO films without noticeable impurity phases, as featured in Figure 1a. We calculated the (001)-oriented films to have an out-of-plane lattice parameter of c = 3.849 (±6) Å (Part I in the Supporting Information). Local ω rocking curves at (001) reflection exhibited a sharp peak together with a broad background peak, indicating that the films were grown by a Stransky−Krastanov growth. Initially adatoms grew in a layer-by-layer fashion, resulting in a sharp peak with a narrow full width at half-maximum of ∼0.03 degree (insets of Figures 1a, and S1), and then growth continued through the nucleation and coalescence of islands. Consequently, it is expected that the misfit strain with the substrate is partially relaxed. We performed

https://doi.org/10.1021/acsnano.3c06675
ACS Nano 2024, 18, 1948−1957

RSM to examine the strain relaxation tendency and determine the crystal structure with in-plane lattice parameters for the thicker film. As expected, epitaxial BCFO films with a pseudotetragonal phase were coherently strained in-plane to match exactly that of STO in RSMs.[18,20] Compared to the vertical alignment of the near-symmetric (002) peak, a slight right-shifted near-asymmetric (113) peak confirms the in-plane lattice parameter is relaxed (Figure 1b). As a direct result of epitaxial BCFO from HAADF-STEM, oxygen-deficient layers (V_O channel) align parallel to the [$\bar{1}$10]-orientation alternating with highly distorted chains of vertex-connected tetrahedra, with a lattice periodicity of 3 in x_{Ca} = 0.6.[7] Finally, the surface topographical images were characterized by atomic force microscopy (AFM) in a scan area of 5 μm × 5 μm (Figure S4). All results yield low root-mean-square roughness (<0.3 nm) without any grain-like structures, whether with or without the SRO layer. Clearly, atomic step terraces appeared in BCFO epitaxial films, consistent with prior results.[20,26,39] However, when the thickness exceeded 50 nm, this phenomenon vanished, while at the same time the surfaces remained significantly flat even with increased thickness. This low surface roughness is a clear indicator of a high-quality epitaxial growth.

Initially, we used normal AFM to investigate possible changes in the sample structure and define corresponding limits of applied bias. We first described the electronic modulation of BCFO using cAFM technology. Micrometer-sized regions were poled in the BCFO layer using a conductive nitrogen-doped diamond-coated silicon tip with an SRO bottom contact, as schematized in the inset of Figure 2a. Unlike its parent $BiFeO_3$, which is better known for its ferroelectric properties, the piezoelectricity was no longer detected with the pseudotetragonal structure (x_{Ca} = 0.6).[18,40] However, the point I−V curve by sweeping the tip bias between ±10 V presents the distinct hysteresis property and typically asymmetric shape corresponding to resistive-switching and rectifying behaviors[41] (Figure 2a). It was set to high conductance with the threshold of −3.8 V and degraded to a low-conductance state below V_{bias} = −1.6 V. This modulation of the transport property was replicated on many samples.

Switching in this bias interval did not change the surface topography, and this low-voltage regime hence is referred to as electronic-state switching behavior. To avoid the dielectric breakdown during the poling process, the surface topography was monitored together. Specifically, we applied a switching voltage U_{tip} (±10 V) between the bottom electrode and the conductive SPM tip. Depending on the amplitude and polarity of the bias, two types of associated changes were observed. First, electronic modulation and switching were observed once the tip was biased. Under the applied bias, the enhanced electrical conductivity and its surface morphology were observed directly in Figure 2b and c. To define the local change on ionic motion, line profiles covering poling current and topographical height obtained in Figure 2b are shown in c. As can be seen, a gradual current increase was observed during the poling process as the bias rose from 0 to −10 V. And, the significant change in the surface topography refers to an additional expansion of lattice unit cells, which was attributed to the electrochemical reaction of V_O motion generally: a large number of V_Os were driven under the negative bias (the bottom electrode of SRO was grounded) and then accumulated at the surface; this strain was modulated electrically with the amplitude of bias. Second, in one poled region under the application of relatively negative voltages, U_{tip} = −10 V, its local current was measured with a reading bias of −2.0 V. The larger concentration of V_Os at the poled-region surface indexed an increased local conductivity, where its readout of current reached ∼0.8 μA under the tip bias of −10 V. On the contrary, the current was suppressed unsurprisingly with the tip bias of +10 V. Their cAFMs are shown in Figure 2d and e, respectively. As the sample was biased, mobile electronic donor V_Os are redistributed and break the compensation with the uniform distribution of acceptor Ca^{2+} ions, generating conducting states locally.[18] A large current contrast gradually appeared compared with that of the initial insulating host, and hence V_Os migrated along the applied field, indicating an onset of the electronic phase transition to a highly conducting state.[42] Simply put, a tip-induced electrical field (∼kV mm^{-1}, which is sufficiently large) drives charged species to move and then causes base element redistribution. In the case of BCFO, the negatively biased tip forces the ionized V_Os (positive charges) to pile up on the surface, simultaneously driving enriched oxygen (O^{2-}) downward. Conversely, a positively biased tip produces the opposite effect, as schematized in Figure 2f.

TOF-SIMS measurements allow us to obtain visual results of associated changes in chemical composition.[34,43] Due to the larger intensity of negatively charged species, particularly O^- ions, we observed saturated trajectories in our experiments. Consequently, the TOF-SIMS experiments described herein were optimized for the detection of positive secondary ions. This mode that we used does not allow us to directly measure the concentration of O^- ions, of course. Oxygen-containing clusters, however, can give rich information regarding the local O^- concentration. In our experiments, a Cs^+ ion gun was used separately as a sputtering source to excite Cs clusters, thereafter forming objective Cs_2O^+ species instead of the intrinsically electronegative O^- ions.

The prominent role of the V_Os and evolution of the local conductivity are clearly demonstrated when studying a multilayer junction of BCFO(230 nm)/SRO(20 nm)/STO. A secondary ions mass spectrum averaged over the whole detected region (100 μm × 100 μm) is presented clearly in Figure 3a, showing the presence of almost all base elements (Ca^+, Fe^+, Bi^+, Ru^+, Ti^+, and Sr^+) and proton-containing species (e.g., H^+), where they are investigated to evaluate chemical reactions under external polarity modulation. Besides, the preferential clusters $CsFe^+$ and $CsBi^+$ may be detected.[14] However, the intensity of Bi^+ is quite small in detectability due to the low concentration in solutions (Bi:Ca = 0.4:0.6) and possibly because of the relatively low ionization ratio under sputtering conditions. Furthermore, we assume that the etching rate is polarization-independent and then calculate it with ∼0.8 nm (2 u.c.) per etching layer in the BCFO layer and ∼1 nm per etching layer in the SRO layer. For reliable analysis, the lattice expansion from additional bias-modulated strain is ignored, where the crystal layer between poled and unpoled regions is the same for TOF-SIMS slices. At the same time, those grain- and cluster-like structures are neglected again for inherent analysis.

Next we investigate changes in chemical composition, especially focusing on oxygen underneath a biased tip. The applied field from a polarity tip was used to produce changes in BCFO/SRO/STO through electroformation. For the regions analyzed in TOF-SIMS, two 10 μm × 10 μm boxes were poled with a bias of −10 and +10 V, successively. We plot the depth profiles of them and a pristine (unpoled) region with the same size, as schematized in Figure 3b and c. The expected depth profiles of base components in TOF-SIMS reveal distinct differences at interfaces (Figure 3c and Figure S10 in the

https://doi.org/10.1021/acsnano.3c06675
ACS Nano 2024, 18, 1948−1957

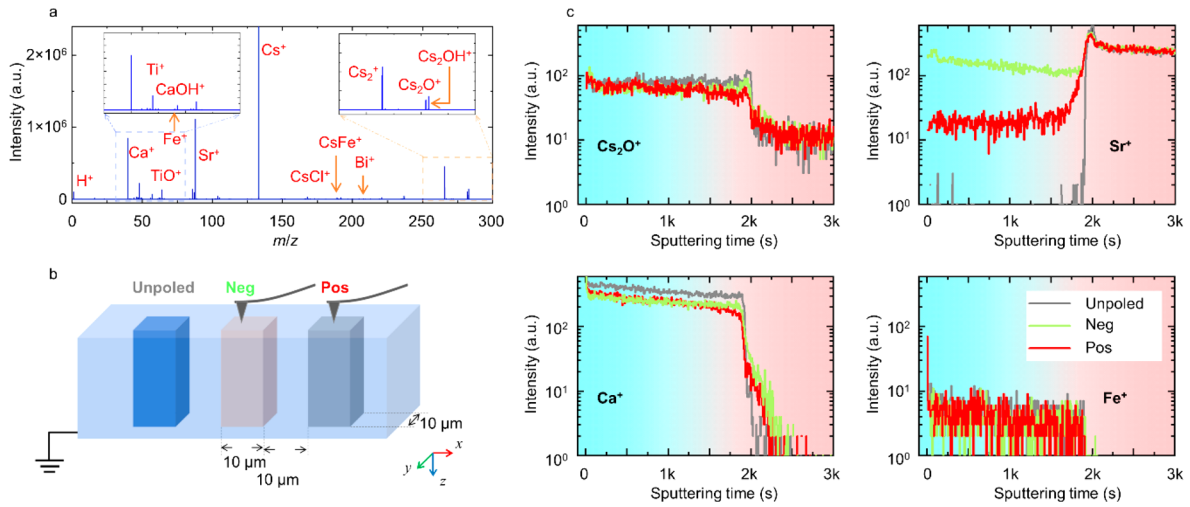

Figure 3. SIMS results of BCFO. (a) Mass spectrum of averaged 3D SIMS scan. (b) Schematic patterns of pristine and poled regions, each measuring 10 μm, with the entire etching region for TOF-SIMS measuring 100 μm. Two regions are poled successively. (c) Depth profiles for targeted species in pristine (gray) and projected (green: −10 V and red: +10 V, respectively) regions.

Supporting Information), where Ca^+ and Fe^+ are found in the BCFO layer, Ru^+ is exclusively in the SRO layer, and Ti^+ is solely in the STO substrate. In addition, Sr^+ clusters are found in SRO and STO together. Their intensities, however, differ greatly due to various etching rates in BCFO and SRO layers. Moreover, all line profiles on Cs_2O^+, Sr^+, Ca^+, and Fe^+ present similar changes but with modulated intensity of the first two. The slopes of Cs_2O^+ of different polarities are different, and Sr^+ appears in the BCFO layer with significantly varying intensity.

The variation in local concentrations can be further evaluated by line and depth profile analysis. Two line profiles passing through separated poled regions provide additional insights into the migration and redistribution of lattice oxygen, as detailed in Figure 4a. The normalized Cs_2O^+ signal, despite the poor signal-to-noise ratio, differs substantially from one scan to the next. This result with different responses is registered at negative and positive tip biases, respectively. The discrepancy is attributed to the corresponding modulation in Cs_2O^+ concentration encountered at different tip polarity. Their concentrations were found to be significantly lower with different depths in BCFO, which indicates a modified decrease of the film in poled areas, confirming the presence of V_Os and the signature of ionic motions. (i) As expected in the region experienced by U_{tip} = +10 V, the canyon-shaped portraits of Cs_2O^+ concentration are observed from a middle layer to deeper ones, indicating the reducing of oxygen ions. Moreover, a swamp of Cs_2O^+-reduced distribution is immersed in the bottom layer, demonstrating an upward motion of oxygen ions driven by the electrostatic force between the biased tip and bottom electrode. At the same time, broader valley-shaped distributions suggest the possibility of lateral diffusion. The absence of a discernible rise in oxygen content on the BCFO film's top surface has us considering the possibility of oxygen expulsion through the material's surface. (ii) Furthermore, the left profile shows the region prepared by U_{tip} = −10 V also undergoes an oxygen decrease similarly, but the concentration variation of Cs_2O^+ is relatively uniform in different depths including the low-depth layers of the film. While there is a notably slight increase in the bottom layer of the BCFO corresponding to a great concentration of oxygen embedded in crystal layers, importantly, a saddle-like change appears in the STO layer underneath a negatively biased tip accidentally. In adjacent areas that can be verified, no notable increase was observed. We believe that the migrated oxygen moving downwardly without accumulation at the bottom layer of the BCFO, however, passes through the SRO conducting layer and further diffuses into the STO substrate, which is in great agreement with the tracer diffusion of oxygen in the $SrTiO_3$ crystal.[44]

Three-dimensional cross-sectional maps give us a clearer visualization of this contrast, as shown in Figure 4b. Notably, chemical imaging reveals that the contrast differs hugely along the z-direction, where different polarities of applied bias demonstrate considerable modulation of the surface Cs_2O^+ concentration. Significantly, an increase in the Cs_2O^+ concentration on the top layer was observed regardless of different polarities, which is, once again, consistent with the above findings. We further generated two-dimensional maps depicting the Cs_2O^+ spatial distribution (middle and right ones in Figure 4c, respectively). Additionally, an unpoled map is presented in Figure 4c (left) for comparison. The raw results are displayed in Figure S8 with an unavoidably inhomogeneous background, which originates from the dispersion of flight time with the increase of etching depth (Part III in the Supporting Information). After subtracting it, the spatial distributions were revealed in the y−z plane, and relative line profiles are displayed further in Figure 4d, obtained by averaging the Cs_2O^+ concentration maps along the vertical direction. Here the oxygen-enriched surface layers were disregarded due to their reactivity in the ambient air environment.[35] Negatively charged O^{2-} species were repulsed from the tip, producing the depletion region on the sample surface and injecting deep into the film. The result we see is that, under the negatively polarized bias, there is a downward trend from bottom to top, and a lower concentration of Cs_2O^+ is detected among the top layers, meaning a large number of V_Os replaced the preferable lattice oxygen (O^{2-}) there. In contrast, a noticeable upward trend line is observed under a positively polarized bias. The lower intensity of Cs_2O^+ corresponds to a higher concentration of V_Os, which further contributes to the observed bias-induced switching asymmetries. Moreover, no noticeable difference was observed in the pristine (unpoled) region at any depths. All of them clearly demonstrated the motion of V_Os under a polarity-biased tip and

https://doi.org/10.1021/acsnano.3c06675
ACS Nano 2024, 18, 1948−1957

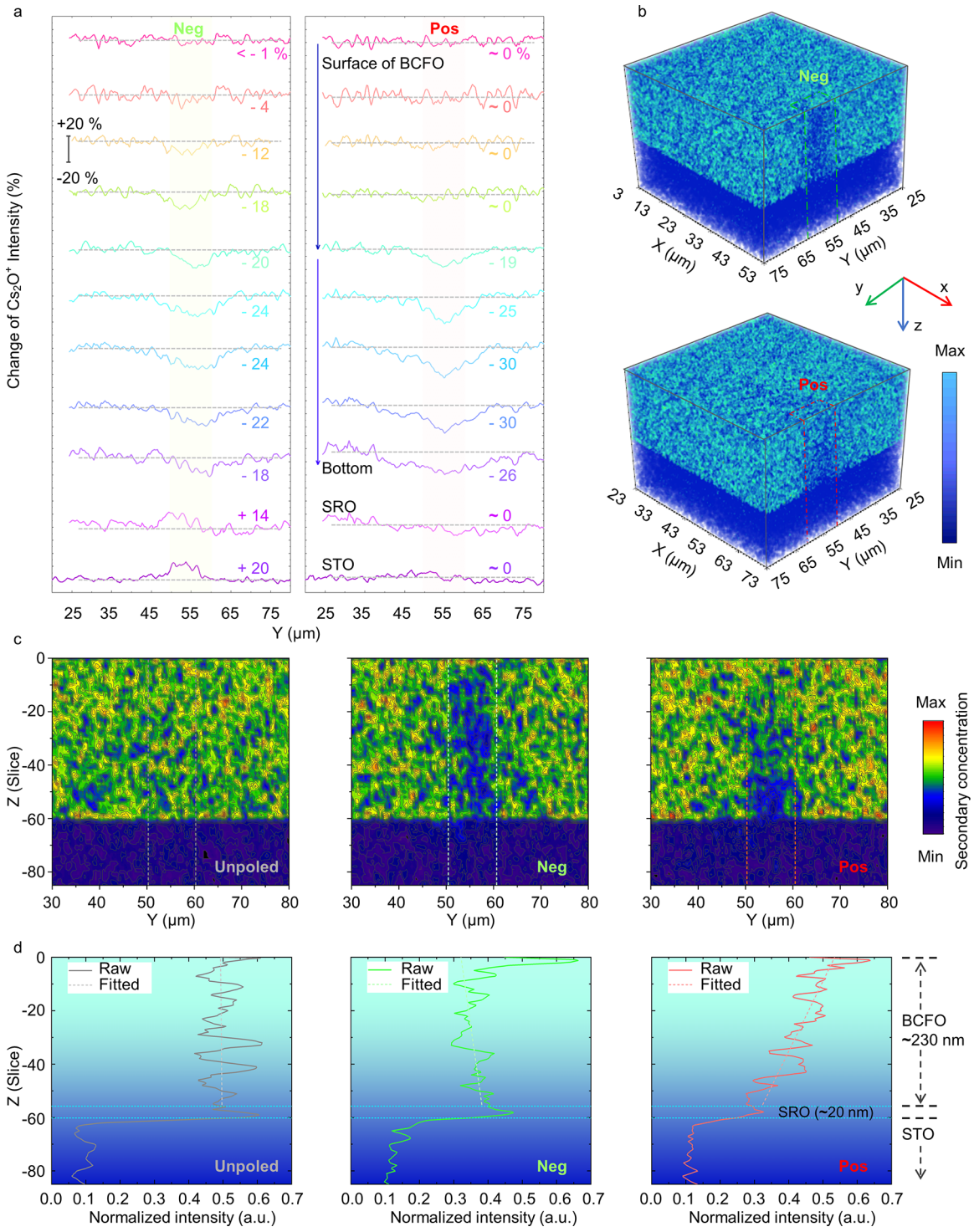

Figure 4. Detailed analysis of Cs_2O^+ ion distribution in SIMS results. (a) Line profiles of Cs_2O^+ concentration at different depths along poled areas, by averaging them along the *x*-axis. Corresponding changes were labeled as percentages based on the differences between baselines and valleys or peaks (detailed analysis with error bars is shown in Figure S9). (b) 3D overlayers of poled regions (upper: − 10 V and lower: +10 V, respectively), showing the huge contrast of spatial distribution upon different polarity biases. (c) Cross sections along the *y*−*z* plane in both poled and pristine regions. (d) Corresponding depth profiles in different regions, which are plotted by averaging measurements within labeled regions. Note that the surface is oxygen-enriched due to exposure to ambient air, and grain-like structures have been disregarded in the analysis.

effectively visualized the accumulation of V_Os near the negatively applied bias.

To fully analyze and understand the spatial chemical element distribution, we plotted two-dimensional and three-dimensional maps of detected species, respectively. Reconstructed maps of Cs_2O^+ in different depths are visualized distinctly in Figure 5a, covering two electroformed regions with different polarization. We discussed that due to the chemical reactivity, the surface was enriched by oxygen and then relaxed completely among poled regions. In deep layers, a huge contrast and opposite trends among them emerged considerably. The higher concentration in the surface of positive- or negative-charged ions and the gradient

https://doi.org/10.1021/acsnano.3c06675
ACS Nano 2024, 18, 1948−1957

distribution along the z-direction presumably originates from bias-assisted kinetic ionic migration.[45]

Furthermore, an unexpected phenomenon was observed at the spatial gap between two poled regions, by accident, as illustrated in Figure 5b, where only a very low concentration of Cs_2O^+ species was detected. Compared to two projected regions with the size of 10 μm, it seems that oversized regions experienced electronic modulation as imaged. The poor intensity that we observed means most of the oxygen-containing species among this region were ejected out. The above result cannot be simply explained in terms of the electrostatic effect under a biased tip, as in this case no electrostatic repulsive or attractive force is attributed to the depletion region of Cs_2O^+ species because it is located far from the poled regions (10 μm of lateral gap). This chemical change is likely to be caused by the huge spatial difference of V_O concentration in the $x-y$ plane, which is determined by Fick's diffusion law, exhibiting desirable lateral diffusion. The bias-induced field attracts more defects accumulating near the surface, while it relaxes and laterally migrates along the ⟨110⟩-oriented periodic V_O channel.[7] The projected region was found to be enlarged by 2−3 μm, and we note that the time gap between the poling process of cAFM and signal collection of TOF-SIMS was about <10 h, so the estimated diffusion constant was about 10^{-12} cm^2 s^{-1} at room temperature, which is 3 orders of a magnitude larger than the reported value (only ~10^{-15} cm^2 s^{-1}).[7,46] Meanwhile, the Joule thermal effect for an increase in body temperature was ignored (Part VI in the Supporting Information). Thus, this enhancement can be attributed to an unclarified conductivity mechanism at room temperature. On the one hand, the immediate tail effect of continuous pulses facilitates the gradual relaxation of local potential even after the electric pulse subsides to zero. Consequently, the ionic motion becomes energetically favorable over short distances as well.[47] On the other hand, highly disordered, strained lattices were observed in electroformed BCFO with a relatively higher concentration of V_O defects,[10] where strain-enhanced diffusion rapidly occurs above the intrinsic concentration of V_Os due to the flexoelectric effect.[48] This enhanced diffusivity was also observed in our real-time recording videos; that is, the ionic mobility in the dark-colored phase (greater concentration of V_Os) is larger than that of the intermediate phase close to room temperature.[7] Thus, their contributions together facilitate the systems relaxing to a lower concentration state from the local accumulation (larger concentration of V_Os), and the migration of V_Os toward the area that was unpoled initially but adjacent to the poled ones manifests a state of temporary nonequilibrium.

Clearly, this model supports only isotropic ionic motion. However, Figure 5a and b focus on the lateral diffusion only appearing along the $x-z$ plane, modeling the anisotropic transport of V_Os at room temperature. This disagreement shows that the simple model described above cannot completely describe this behavior. A more precise model should incorporate electromigration as a self-consistent problem based on electrostatics,[38] where induced-field $\boldsymbol{E}_{ind}$ originates from ionic motion changing the local distribution ($\boldsymbol{E}_{ind} = \boldsymbol{E}(n, \boldsymbol{r}, t)$, where n, $\boldsymbol{r}$, and t represent the accumulated charge density, relative spatial distance, and relative time scale, respectively (see Part VII in the Supporting Information)). To obtain a numerical simulation of the gradient-composition-induced electric field, a model of layer-by-layer dipoles is applied for electrostatic potential (Figure 5c). Due to a gradient distribution of accumulated charges, the static electric field is strongly enhanced along the inner region with a nonequilibrium contribution, dominating the acceleration of V_O drift in the $+x$-direction.[46] Such advanced simulation on relaxation including a time-dependent Poisson equation is beyond the scope of the current work and will be further studied elsewhere.

In addition to the motion of V_Os, the electric polarization also denotes significant changes of chemical compositions; for example, the degradation of a ferroelectric film induced by a larger bias was confirmed by irreversible damage in topography, mainly originating from the redistribution of base cations from the bottom layer into $BiFeO_3$.[14] Here to gain a comprehensive understanding of chemical evolution under a negatively biased tip, we present a three-dimensional overlay visualizing Sr^+ (cyan), Ca^+ (coral), Fe^+ (silver), and Ti^+ (purple) ions (Bi^+ and Ru^+ are not shown here due to their minimal intensities; the shades of the typical colors denote species concentration). This visualization covers a 10 × 10 μm cross section under $U_{tip} = -10$ V, as illustrated in Figure 5d and Figure S10. No structural damage in the AFM topography is indicated after the electrical poling process. Detailed analysis of different cations featured significant cations intermixing between the BCFO and SRO layers, bringing about the penetration of alkaline-earth cation Sr^+ into the BCFO layer, which strongly agrees with the polarity of the applied electric field. Our result, however, could not produce evidence that Fe^+ ions penetrated deeply into the bottom layers associated with polarization due to the extremely weak contrast in a positively biased region. The introduction of the positively charged species Sr^+ by electrostatic attraction between a negatively biased tip and the grounded bottom layer can be discussed further. This redistribution of cations among multilayers results in a metastable state with a tunable composition of $(Bi,Ca,Sr)FeO_{3-\beta}$, where it is difficult to determine the accurate atomic ratio experimentally. It only supports the motion of Sr^+ under a polarity bias from our TOF-SIMS results, and the estimated mobility is about 2 × 10^{-13} cm^2 s^{-1}, which is also three orders of an amplitude larger than the value reported in previous work.[49]

CONCLUSIONS

In summary, we have realized the 3D visualization of ionic redistribution in epitaxial BCFO films with the electrochemical modification of local transport. Without any intrinsically ferroelectric property, BCFO with a doping ratio of $x_{Ca} = 0.6$ is ionic, which allows us to study the evolution of the iontronic properties. With the mediation of creation and annihilation of V_Os, the surface electronic conductivity and compositional distribution are locally regulated through a biased tip during the electrochemical reaction. Thus, through the combined study of cAFM and TOF-SIMS, we utilize the electrical polarity to manipulate the local conductivity in BCFO films. We observe the opposite-trend migration of V_Os in real space, pinpointed down to a nanometer scale through electric bias, attributed to the electrostatically attractive/repulsive force of V_O/lattice-oxygen beneath the SPM tip. Moreover, our experimental findings reveal unexplored room-temperature diffusion enhancement of V_Os with a spatially anisotropic feature, which is dominated by the combined effects of the induced electrostatic potential and highly strained lattices. Our results display the strong coupling between ionic motion, local strain, and surface conductivity, thereby providing valuable insights into the mechanisms underlying ionic conductors and multistate memory behaviors for the development of next-generation electronic/electrochromic devices.

https://doi.org/10.1021/acsnano.3c06675
ACS Nano 2024, 18, 1948−1957

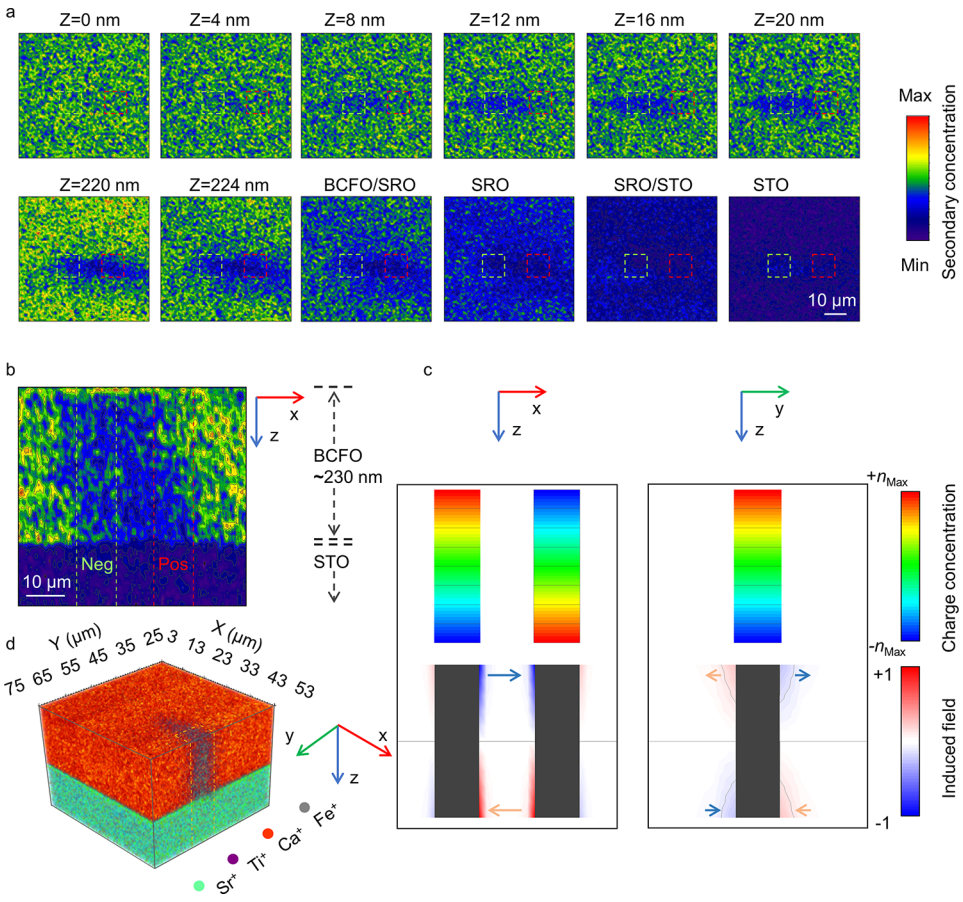

Figure 5. Spatial distribution of detected species. (a) Chemical maps of the *x*-*y* spatial distribution of Cs_2O^+ at different depths, normalized to the maximum intensity. To gain a clear understanding of spatial differences, each slice includes all information from a 4-nm-thick layer (approximately 8 u.c.). The green and red edge-colored squares indicate the polarity regions with biases of −10 V and +10 V, respectively. The color of dark blue, green, yellow, and red indicate the relative concentration varying from lower to higher. (b) Profile of the Cs_2O^+ species in the *x*−*z* plane, where the lateral spatial gap between poled regions is 10 μm. (c) The simulated static electric field *E* with gradient charges, showing the in-plane induced field E_{ip} is enhanced in the lateral gap and anisotropic between the *x*−*z* and *y*−*z* planes. (d) 3D overlayer of Sr^+ (cyan), Ca^+ (coral), Fe^+ (silver), and Ti^+ (purple) ions (Bi^+ and Ru^+ are not plotted visually due to their minimal intensities). The shade of color represents the concentration of the species. Cross-sectional 2D maps are shown in Figure S10. The unit in spatial scale is μm.

METHODS

Thin Film Depositions. In our experiment, the BCFO films were deposited on (001) STO single crystals (CrysTec GmbH) by using pulsed laser deposition. A KrF excimer laser with a wavelength of 248 nm was used for their epitaxial growth. The custom-made targets were calcinated using the conventional solid-phase reaction method, and details of the procedure can be found in refs 20, 26, and 50. After ultrasonically being cleaned and then being transferred into the chamber, the STO single crystal was annealed at 675 °C in oxygen gas of 150 mTorr during the whole deposition process. The optimized laser conditions for epitaxial growth were a laser intensity of 1.2 J cm^{-2} and a laser repetition frequency of 10 Hz, with the estimated growth rate of 1.4 nm min^{-1}.

For cAFM measurements, a conducting $SrRuO_3$ layer with a thickness of 20 nm was initially grown at a substrate temperature of 700 °C and an oxygen pressure of 150 mTorr. It resulted in a ∼20-nm-thick SRO layer with 6000 laser pulses.

Structural Characterizations. To analyze the crystal structure of the epitaxial Ca-doped $BiFeO_3$ thin film, XRD with conventional 2θ–ω scans and RSMs were taken using a commercial PANalytical X'Pert-PRO MRD diffractometer with Cu $K\alpha_1$ radiation (λ = 1.5406 Å).

AFM and cAFM measurements were performed at room temperature using a Bruker scanning probe microscopy instrument (Multi Mode-V HR). The topography was mapped using a standard silicon tip (μmasch) with an area of 5 μm × 5 μm. For cAFM experiments, a conductive diamond-coated silicon tip (nitrogen-doped, CDT-FMR-SPL, NanoWorld) with a force constant of 6.2 N m^{-1} was used, where it was equipped with a cAFM application module (TUNA). Standard boxing−poling processes were done with a size of 3 μm, while the current of the poled regions was monitored. The topography was also monitored to ensure that there was no structural damage. Poling was completed when the current reached about 1 μA. The typical scanning rate was 0.3 μm s^{-1}. All data were obtained under ambient conditions at room temperature.

Time-of-Flight Secondary Ion Mass Spectrometry. For the regions analyzed in TOF-SIMS, two 10 μm × 10 μm boxes were poled with a trial-and-error method with a bias of −10 and +10 V, respectively. During the poling process, scanning 10 μm required 512 points at a rate of 0.2 Hz. It took approximately 3 h for every region to complete the poling procedure successfully.

Mass spectrometry measurements were collected using a TOF SIMS-5 instrument (ION-TOF GmbH, Germany). Here the positive ion detection mode with tracking the Cs_2O^+ mass peak was regarded experimentally as the typical fingerprint of oxygen content. In these measurements, surface layers were bombarded continuously by a focused Bi^{3+} beam, and the released secondary positive ions were detected and identified by using a time-of-flight detector. The primary beam with a 30 keV Bi ion gun was spotted on an area with a size of 100 μm × 100 μm. The sputter beam was set at 1 keV and 50 nA for a Cs^+ ion-sputtering source over a 300 μm total area. The analysis was done using a cycle time of 100 μs in random mode, with an image resolution of 256 × 256 pixels. *Ex situ* AFM calibration after sputtering revealed an

https://doi.org/10.1021/acsnano.3c06675
ACS Nano 2024, 18, 1948−1957

etching rate of about 0.8 nm (2 u.c.) per etching layer in BCFO. Two 10-μm-sized regions were initially poled under tip biases of −10 and +10 V, respectively, with a lateral spatial distance of 10 μm.

ASSOCIATED CONTENT

Supporting Information

The Supporting Information is available free of charge at https://pubs.acs.org/doi/10.1021/acsnano.3c06675.

Detailed analysis of XRD results and AFMs (Figures S1−S4 and Table S1); growth of conducting layers of $SrRuO_3$ (Figure S5 and Table S2); inhomogeneous distribution vs dispersion of flight time in TOF-SIMS (Figures S6, S7); subtraction of inhomogeneous background in depth profiles for TOF-SIMS (Figure S8); additional discussion of TOF-SIMS results (Figures S9, S10); Joule heating effect; gradient-composition-induced field (Figure S11) (PDF)

AUTHOR INFORMATION

Corresponding Author

Chan-Ho Yang − *Department of Physics and Center for Lattice Defectronics, KAIST, Daejeon 34141, Republic of Korea; KAIST Institute for the NanoCentury, Korea Advanced Institute of Science and Technology, Daejeon 34141, Republic of Korea;* orcid.org/0000-0002-3384-4272; Email: chyang@kaist.ac.kr

Authors

Bingqian Song − *Department of Physics and Center for Lattice Defectronics, KAIST, Daejeon 34141, Republic of Korea;* orcid.org/0009-0007-3034-0988

Heung-Sik Park − *Department of Physics and Center for Lattice Defectronics, KAIST, Daejeon 34141, Republic of Korea;* orcid.org/0000-0003-1067-268X

Jeonghun Suh − *Department of Physics and Center for Lattice Defectronics, KAIST, Daejeon 34141, Republic of Korea*

Jeongdae Seo − *Department of Physics and Center for Lattice Defectronics, KAIST, Daejeon 34141, Republic of Korea*

Jihun Kim − *Department of Physics and Center for Lattice Defectronics, KAIST, Daejeon 34141, Republic of Korea*

Complete contact information is available at: https://pubs.acs.org/10.1021/acsnano.3c06675

Author Contributions

B.S., H.-S.P., and C.-H.Y. conceived and designed the project. B.S. and J.S. prepared the samples and performed XRD characterization. B.S. and J.K. measured and analyzed cAFM data. B.S. and H.-S.P. carried out and analyzed TOF-SIMS. J.S. shared the explanation on abnormal spatial contributions, and B.S. performed induced-field simulations for the spatially gradient distribution of oxygen vacancies. B.S. and C.-H.Y. wrote the manuscript based on the above contributions and fruitful discussions.

Notes

The authors declare no competing financial interest.

ACKNOWLEDGMENTS

We are grateful for the fruitful discussions with Dr. Christian Muhmann (IONTOF Support, Germany). This work is financially supported by National Research Foundation grants in Korea via the Creative Research Initiative Center for Lattice Defectronics (2017R1A3B1023686).

REFERENCES

(1) Lu, N.; Zhang, P.; Zhang, Q.; Qiao, R.; He, Q.; Li, H. B.; Wang, Y.; Guo, J.; Zhang, D.; Duan, Z.; Li, Z.; Wang, M.; Yang, S.; Yan, M.; Arenholz, E.; Zhou, S.; Yang, W.; Gu, L.; Nan, C. W.; Wu, J.; Tokura, Y.; Yu, P. Electric-Field Control of Tri-State Phase Transformation with a Selective Dual-Ion Switch. *Nature* **2017**, *546* (7656), 124−128.

(2) Seidel, J.; Trassin, M.; Zhang, Y.; Maksymovych, P.; Uhlig, T.; Milde, P.; Köhler, D.; Baddorf, A. P.; Kalinin, S. V.; Eng, L. M.; Pan, X.; Ramesh, R. Electronic Properties of Isosymmetric Phase Boundaries in Highly Strained Ca-Doped $BiFeO_3$. *Adv. Mater.* **2014**, *26* (25), 4376−4380.

(3) Tuller, H. L.; Bishop, S. R. Point Defects in Oxides: Tailoring Materials through Defect Engineering. *Annu. Rev. Mater. Res.* **2011**, *41*, 369−398.

(4) Geng, W. R.; Tian, X. H.; Jiang, Y. X.; Zhu, Y. L.; Tang, Y. L.; Wang, Y. J.; Zou, M. J.; Feng, Y. P.; Wu, B.; Hu, W. T.; Ma, X. L. Unveiling the Pinning Behavior of Charged Domain Walls in $BiFeO_3$ Thin Films via Vacancy Defects. *Acta Mater.* **2020**, *186*, 68−76.

(5) Seidel, J.; Maksymovych, P.; Batra, Y.; Katan, A.; Yang, S. Y.; He, Q.; Baddorf, A. P.; Kalinin, S. V.; Yang, C. H.; Yang, J. C.; Chu, Y. H.; Salje, E. K. H.; Wormeester, H.; Salmeron, M.; Ramesh, R. Domain Wall Conductivity in La-Doped $BiFeO_3$. *Phys. Rev. Lett.* **2010**, *105* (19), No. 107603.

(6) Lim, J. S.; Lee, J.; Lee, B. J.; Kim, Y. J.; Park, H. S.; Suh, J.; Nahm, H. H.; Kim, S. W.; Cho, B. G.; Koo, T. Y.; Choi, E.; Kim, Y. H.; Yang, C. H. Harnessing the Topotactic Transition in Oxide Heterostructures for Fast and High-Efficiency Electrochromic Applications. *Sci. Adv.* **2020**, *6* (41), No. eabb8553.

(7) Lim, J. S.; Nahm, H.; Campanini, M.; Lee, J.; Kim, Y.-J.; Park, H.; Suh, J.; Jung, J.; Yang, Y.; Koo, T. Y.; Rossell, M. D.; Kim, Y.; Yang, C. Critical Ionic Transport across an Oxygen-Vacancy Ordering Transition. *Nat. Commun.* **2022**, *13* (1), 5130.

(8) Kwon, Y. J.; Yeo, Y.; Kim, M. S.; Kim, Y. J.; Park, H. S.; Kim, J.; Choi, S. Y.; Yang, C. H. Observation of Hidden Polar Phases and Flux Closure Domain Topology in Bi_2WO_6 Thin Films. *Nano Lett.* **2023**, *23* (10), 4557−4563.

(9) Wang, L.; Yang, Z.; Bowden, M. E.; Du, Y. Brownmillerite Phase Formation and Evolution in Epitaxial Strontium Ferrite Heterostructures. *Appl. Phys. Lett.* **2019**, *114* (23), No. 231602.

(10) Park, H. S.; Lim, J. S.; Suh, J.; Yang, C. H. Electric-Field-Induced Epitaxial Breakdown and Emergent Magnetoresistance Due to Strong Oxygen Reduction in Ca-Doped $BiFeO_3$. *Phys. Rev. Mater.* **2022**, *6* (2), 24404.

(11) Ikeda-Ohno, A.; Lim, J. S.; Ohkochi, T.; Yang, C. H.; Seidel, J. Investigation of Continuous Changes in the Electric-Field-Induced Electronic State in $Bi_{1-x}Ca_xFeO_{3-\delta}$. *Phys. Chem. Chem. Phys.* **2014**, *16* (33), 17412−17416.

(12) Wang, X.; Song, B.; Tao, L. L.; Wen, J.; Zhang, L.; Zhang, Y.; Lv, Z.; Tang, J.; Sui, Y.; Song, B.; Han, X. F. Effect of a Semiconductor Electrode on the Tunneling Electroresistance in Ferroelectric Tunneling Junction. *Appl. Phys. Lett.* **2016**, *109* (16), No. 163501.

(13) Kilner, J. A.; Brook, R. J. A Study of Oxygen Ion Conductivity in Doped Non-Stoichiometric Oxides. *Solid State Ion.* **1982**, *6* (3), 237−252.

(14) Ievlev, A. V.; Maksymovych, P.; Trassin, M.; Seidel, J.; Ramesh, R.; Kalinin, S. V.; Ovchinnikova, O. S. Chemical State Evolution in Ferroelectric Films during Tip-Induced Polarization and Electroresistive Switching. *ACS Appl. Mater. Interfaces* **2016**, *8* (43), 29588−29593.

(15) Lindgren, G.; Ievlev, A.; Jesse, S.; Ovchinnikova, O. S.; Kalinin, S. V.; Vasudevan, R. K.; Canalias, C. Elasticity Modulation Due to Polarization Reversal and Ionic Motion in the Ferroelectric Superionic Conductor $KTiOPO_4$. *ACS Appl. Mater. Interfaces* **2018**, *10* (38), 32298−32303.

(16) Inoue, S.; Kawai, M.; Ichikawa, N.; Kageyama, H.; Paulus, W.; Shimakawa, Y. Anisotropic Oxygen Diffusion at Low Temperature in Perovskite-Structure Iron Oxides. *Nat. Chem.* **2010**, *2* (3), 213−217.

(17) Zeches, R. J.; Rossell, M. D.; Zhang, J. X.; Hatt, A. J.; He, Q.; Yang, C.-H.; Kumar, A.; Wang, C. H.; Melville, A.; Adamo, C.; Sheng,

G.; Chu, Y.-H.; Ihlefeld, J. F.; Erni, R.; Ederer, C.; Gopalan, V.; Chen, L. Q.; Schlom, D. G.; Spaldin, N. A.; Martin, L. W.; Ramesh, R. A Strain-Driven Morphotropic Phase Boundary in $BiFeO_3$. *Science* **2009**, *326* (13), 977−980.
(18) Yang, C. H.; Seidel, J.; Kim, S. Y.; Rossen, P. B.; Yu, P.; Gajek, M.; Chu, Y. H.; Martin, L. W.; Holcomb, M. B.; He, Q.; Maksymovych, P.; Balke, N.; Kalinin, S. V.; Baddorf, A. P.; Basu, S. R.; Scullin, M. L.; Ramesh, R. Electric Modulation of Conduction in Multiferroic Ca-Doped $BiFeO_3$ Films. *Nat. Mater.* **2009**, *8* (6), 485−493.
(19) Jethva, S.; Katba, S.; Bhatnagar, M.; Ranjan, M.; Shukla, D.; Kuberkar, D. G. Effect of Strain on the Modifications in Electronic Structure and Resistive Switching in Ca-Doped $BiFeO_3$ Films. *J. Appl. Phys.* **2019**, *125* (8), No. 082510.
(20) Lim, J. S.; Lee, J. H.; Park, H. S.; Gao, R.; Koo, T. Y.; Martin, L. W.; Ramesh, R.; Yang, C. H. Ultrafast Collective Oxygen-Vacancy Flow in Ca-Doped $BiFeO_3$. *NPG Asia Mater.* **2018**, *10* (9), 943−955.
(21) Xiao, C. F.; Kim, J. H.; Cho, S. H.; Park, Y. C.; Kim, M. J.; Chung, K. B.; Yoon, S. G.; Jung, J. W.; Kim, I. D.; Kim, H. S. Ensemble Design of Electrode-Electrolyte Interfaces: Toward High-Performance Thin-Film All-Solid-State Li-Metal Batteries. *ACS Nano* **2021**, *15* (3), 4561−4575.
(22) Yaguchi, H.; Morikawa, D.; Saito, T.; Tsuda, K.; Yashima, M. High Oxide-Ion Conductivity through the Interstitial Oxygen Site in Sillén Oxychlorides. *Adv. Funct. Mater.* **2023**, *33*, 2214082.
(23) Cherry, M.; Islam, M. S.; Catlow, C. R. A. Oxygen Ion Migration in Perovskite-Type Oxides. *J. Solid State Chem.* **1995**, *118*, 125.
(24) Masó, N.; West, A. R. Electrical Properties of Ca-Doped $BiFeO_3$ Ceramics: From p-Type Semiconduction to Oxide-Ion Conduction. *Chem. Mater.* **2012**, *24* (11), 2127−2132.
(25) Szot, K.; Speier, W.; Bihlmayer, G.; Waser, R. Switching the Electrical Resistance of Individual Dislocations in Single-Crystalline $SrTiO_3$. *Nat. Mater.* **2006**, *5* (4), 312−320.
(26) Park, H. S.; Lim, J. S.; Suh, J.; Yang, C. H. Real-Time Observation of Filamentary Conduction Pathways in Ca-Doped $BiFeO_3$. *Appl. Phys. Lett.* **2019**, *115* (18), No. 183901.
(27) Liao, Z.; Gao, P.; Bai, X.; Chen, D.; Zhang, J. Evidence for Electric-Field-Driven Migration and Diffusion of Oxygen Vacancies in $Pr_{0.7}Ca_{0.3}MnO_3$. *J. Appl. Phys.* **2012**, *111* (11), No. 114506.
(28) Li, M.; Shen, Y.; Luo, K.; An, Q.; Gao, P.; Xiao, P.; Zou, Y. Harnessing Dislocation Motion Using an Electric Field. *Nat. Mater.* **2023**, *22*, 958−963.
(29) Metlenko, V.; Jung, W.; Bishop, S. R.; Tuller, H. L.; De Souza, R. A. Oxygen Diffusion and Surface Exchange in the Mixed Conducting Oxides $SrTi_{1-y}Fe_yO_{3-\delta}$. *Phys. Chem. Chem. Phys.* **2016**, *18* (42), 29495−29505.
(30) Zapata, J.; Burriel, M.; García, P.; Kilner, J. A.; Santiso, J. Anisotropic ^{18}O Tracer Diffusion in Epitaxial Films of $GdBaCo_2O_{5+\delta}$ Cathode Material with Different Orientations. *J. Mater. Chem. A* **2013**, *1* (25), 7408−7414.
(31) Ievlev, A. V.; Kc, S.; Vasudevan, R. K.; Kim, Y.; Lu, X.; Alexe, M.; Cooper, V. R.; Kalinin, S. V.; Ovchinnikova, O. S. Non-Conventional Mechanism of Ferroelectric Fatigue via Cation Migration. *Nat. Commun.* **2019**, *10* (1), 3064.
(32) Sharma, Y.; Balachandran, J.; Sohn, C.; Krogel, J. T.; Ganesh, P.; Collins, L.; Ievlev, A. V.; Li, Q.; Gao, X.; Balke, N.; Ovchinnikova, O. S.; Kalinin, S. V.; Heinonen, O.; Lee, H. N. Nanoscale Control of Oxygen Defects and Metal-Insulator Transition in Epitaxial Vanadium Dioxides. *ACS Nano* **2018**, *12* (7), 7159−7166.
(33) Belianinov, A.; Ievlev, A. V.; Lorenz, M.; Borodinov, N.; Doughty, B.; Kalinin, S. V.; Fernández, F. M.; Ovchinnikova, O. S. Correlated Materials Characterization via Multimodal Chemical and Functional Imaging. *ACS Nano* **2018**, *12* (12), 11798−11818.
(34) Neumayer, S. M.; Ievlev, A. V.; Collins, L.; Vasudevan, R.; Baghban, M. A.; Ovchinnikova, O.; Jesse, S.; Gallo, K.; Rodriguez, B. J.; Kalinin, S. V. Surface Chemistry Controls Anomalous Ferroelectric Behavior in Lithium Niobate. *ACS Appl. Mater. Interfaces* **2018**, *10* (34), 29153−29160.
(35) Domingo, N.; Gaponenko, I.; Cordero-Edwards, K.; Stucki, N.; Pérez-Dieste, V.; Escudero, C.; Pach, E.; Verdaguer, A.; Paruch, P. Surface Charged Species and Electrochemistry of Ferroelectric Thin Films. *Nanoscale* **2019**, *11* (38), 17920−17930.
(36) Ievlev, A. V.; Brown, C.; Burch, M. J.; Agar, J. C.; Velarde, G. A.; Martin, L. W.; Maksymovych, P.; Kalinin, S. V.; Ovchinnikova, O. S. Chemical Phenomena of Atomic Force Microscopy Scanning. *Anal. Chem.* **2018**, *90* (5), 3475−3481.
(37) Ding, X.; Tam, C. C.; Sui, X.; Zhao, Y.; Xu, M.; Choi, J.; Leng, H.; Zhang, J.; Wu, M.; Xiao, H.; Zu, X.; Garcia-Fernandez, M.; Agrestini, S.; Wu, X.; Wang, Q.; Gao, P.; Li, S.; Huang, B.; Zhou, K. J.; Qiao, L. Critical Role of Hydrogen for Superconductivity in Nickelates. *Nature* **2023**, *615* (7950), 50−55.
(38) Ievlev, A. V.; Brown, C. C.; Agar, J. C.; Velarde, G. A.; Martin, L. W.; Belianinov, A.; Maksymovych, P.; Kalinin, S. V.; Ovchinnikova, O. S. Nanoscale Electrochemical Phenomena of Polarization Switching in Ferroelectrics. *ACS Appl. Mater. Interfaces* **2018**, *10* (44), 38217−38222.
(39) Lim, J. S.; Lee, J. H.; Ikeda-Ohno, A.; Ohkochi, T.; Kim, K. S.; Seidel, J.; Yang, C. H. Electric-Field-Induced Insulator to Coulomb Glass Transition via Oxygen-Vacancy Migration in Ca-Doped $BiFeO_3$. *Phys. Rev. B* **2016**, *94* (3), No. 035123.
(40) Seidel, J.; Luo, W.; Suresha, S. J.; Nguyen, P. K.; Lee, A. S.; Kim, S. Y.; Yang, C. H.; Pennycook, S. J.; Pantelides, S. T.; Scott, J. F.; Ramesh, R. Prominent Electrochromism through Vacancy-Order Melting in a Complex Oxide. *Nat. Commun.* **2012**, *3*, 799.
(41) Maksymovych, P.; Seidel, J.; Chu, Y. H.; Wu, P.; Baddorf, A. P.; Chen, L. Q.; Kalinin, S. V.; Ramesh, R. Dynamic Conductivity of Ferroelectric Domain Walls in $BiFeO_3$. *Nano Lett.* **2011**, *11* (5), 1906−1912.
(42) Strelcov, E.; Kim, Y.; Jesse, S.; Cao, Y.; Ivanov, I. N.; Kravchenko, I. I.; Wang, C. H.; Teng, Y. C.; Chen, L. Q.; Chu, Y. H.; Kalinin, S. V. Probing Local Ionic Dynamics in Functional Oxides at the Nanoscale. *Nano Lett.* **2013**, *13* (8), 3455−3462.
(43) Kubicek, M.; Cai, Z.; Ma, W.; Yildiz, B.; Hutter, H.; Fleig, J. Tensile Lattice Strain Accelerates Oxygen Surface Exchange and Diffusion in $La_{1-x}Sr_xCoO_{3-\delta}$ Thin Films. *ACS Nano* **2013**, *7* (4), 3276−3286.
(44) De Souza, R. A. Oxygen Diffusion in $SrTiO_3$ and Related Perovskite Oxides. *Adv. Funct. Mater.* **2015**, *25* (40), 6326−6342.
(45) Yan, M. F.; Cannon, R. M.; Bowen, H. K. Space Charge Distributions near Interfaces during Kinetic Processes. *J. Appl. Phys.* **1983**, *54* (2), 779−791.
(46) Yeo, Y.; Hwang, S. Y.; Yeo, J.; Kim, J.; Jang, J.; Park, H. S.; Kim, Y. J.; Le, D. D.; Song, K.; Kim, M.; Ryu, S.; Choi, S. Y.; Yang, C. H. Configurable Crack Wall Conduction in a Complex Oxide. *Nano Lett.* **2023**, *23* (2), 398−406.
(47) Chien, Y. C.; Liu, H.; Menon, A. S.; Brant, W. R.; Brandell, D.; Lacey, M. J. Rapid Determination of Solid-State Diffusion Coefficients in Li-Based Batteries via Intermittent Current Interruption Method. *Nat. Commun.* **2023**, *14* (1), No. 2289.
(48) Nian, Y. B.; Strozier, J.; Wu, N. J.; Chen, X.; Ignatiev, A. Evidence for an Oxygen Diffusion Model for the Electric Pulse Induced Resistance Change Effect in Transition-Metal Oxides. *Phys. Rev. Lett.* **2007**, *98* (14), No. 146403.
(49) De Sduza, M. F. Effective Volumes of Vacancies of Divalent Ions and Their Diffusion Coefficients in Alkali Halides. *Phys. Rev.* **1969**, *188* (3), 1367−1370.
(50) Suh, J.; Lim, J. S.; Park, H.; Yang, C. Complementary Study of Anisotropic Ion Conduction in (110)-Oriented Ca-Doped $BiFeO_3$ Films Using Electrochromism and Impedance Spectroscopy. *Appl. Phys. Lett.* **2021**, *119*, No. 022902.

https://doi.org/10.1021/acsnano.3c06675
ACS Nano 2024, 18, 1948−1957